Draft version April 1, 2015
Preprint typeset using LaTeX style emulateapj v. 12/16/11

ILLUMINATING A DARK LENS : A TYPE IA SUPERNOVA MAGNIFIED BY GALAXY CLUSTER ABELL 2744

Steven A. Rodney[1,2], et al.

Draft version April 1, 2015

ABSTRACT

SN HFF14Tom is a Type Ia Supernova (SN Ia) discovered at $z = 1.31 \pm 0.01$ behind the galaxy cluster Abell 2744 ($z = 0.308$). This SN has a projected separation from the cluster core of $\sim$40″, closer to the critical lensing line than any previous cluster-lensed SN Ia. As such, it provides the first opportunity to confront gravitational lens models of galaxy clusters with the direct measurement of an absolute magnification at the edge of the strong-lensing region. We derive a tightly constrained measure of the peak apparent magnitude, corrected for light curve shape and exinction. In a cosmology-independent analysis, we find that HFF14Tom is 0.75 ± 0.10 magnitudes brighter than unlensed SNe Ia at similar redshift, implying a lensing magnification of $\mu_{\rm obs} = 2.00 \pm 0.19$. We compare this direct measurement of the magnification against predicted magnifications from 11 lens models, representing a broad range of methodologies and incorporating a variety of strong- and weak-lensing constraints. The models are collectively fairly accurate, with 3 that are consistent within the 1σ uncertainties. However, the models are systematically biased to higher values: none of the tested models predict a magnification equal to or lower than the observed μ, and some models are more than 5σ above the measured magnification. We evaluate possible causes for this bias, and find that intercomparison of the lens models rules out several simple possibilities. A larger sample of $\sim$10 SNe Ia behind any single cluster could provide a robust evaluation of systematic biases in lens models. Until such a sample exists, it is advisable to **increase the estimated uncertainty of predicted magnifications to match the dispersion observed across multiple lens models.**

Keywords: supernovae: general

1. INTRODUCTION

TODO: write and polish introduction. Massive galaxy clusters can be used as cosmic telescopes to magnify distant background objects through gravitational lensing. This can substantially increase the reach of deep imaging surveys, and has recently been used to discover candidate proto-galaxies formed in the first Gyr after the Big Bang (Zheng et al. 2012; Coe et al. 2013) (cite other high-z galaxy candidates discovered with lensing)

TODO: describe past examples of lensed SN studies (Goobar et al. 2009; Riehm et al. 2011; Quimby et al. 2014).

Patel et al. (2014, hereafter P14) and Nordin et al. (2014) presented independent analyses of three lensed SNe, of which at least 2 are securely classified as Type Ia SNe. All of these three objects were found in the Cluster Lensing and Supernova survey with Hubble (CLASH, PI:Postman, HST Program ID 12068).

One of the key values in observing standard candles behind gravitational lenses is that *all* lensing reconstructions suffer from the mass-sheet degeneracy (Falco et al. 1985; Bradač et al. 2004). This degeneracy arises because one can introduce into a lens model an unassociated sheet of mass in front of or behind the lens, without disturbing the primary observable quantities. For example, take a lens model with a given surface mass density κ, and then transform the surface mass density to $\kappa' = (1-\lambda)\kappa + \lambda$ for any arbitrary value λ. Both the κ and κ' models will produce exactly the same values for all positional and shear constraints from strong and weak lensing. This is the simplest case illustrating a positional constraint degeneracy, but there are more complex versions (?). Such mass sheet degeneracies do not extend to the (?) magnification of a background source's flux and size. Therefore, an absolute measurement of magnification from a standard candle or a standard ruler (Sonnenfeld et al. 2011) can break this fundamental degeneracy (Holz 2001).

In Section 2 we present the discovery and follow-up observations of SN HFF14Tomat $z = 1.31$, discovered behind the galaxy cluster Abell 2744. Sections 3 and 4 describe the spectroscopy and photometry of this SN, leading to a classification of the object as a normal Type Ia SN. In Section 5 we make a direct measurement of the magnification of this source due to gravitational lensing, and compare to predictions from lens models. Finally, Section 6 discusses the tension between our magnification measurement and the lens models, with implications for the systematic error budget in magnification estimates for other high-z lensed sources.

2. DISCOVERY, FOLLOW-UP, AND DATA PROCESSING

SN HFF14Tom was discovered in Hubble Space Telescop (*HST*) observations with the Advanced Camera for Surveys (ACS) in the F606W and F814W bands (V and i), collected on UT 2014 May 15 as part of the Hubble Frontier Fields (HFF) survey (PI:J.Lotz, HST-PID:13495).[3] The HFF program is a 3-year director's

[1] Department of Physics and Astronomy, The Johns Hopkins University, Baltimore, MD 21218.
[2] Hubble fellow

[3] `http://www.stsci.edu/hst/campaigns/frontier-fields`

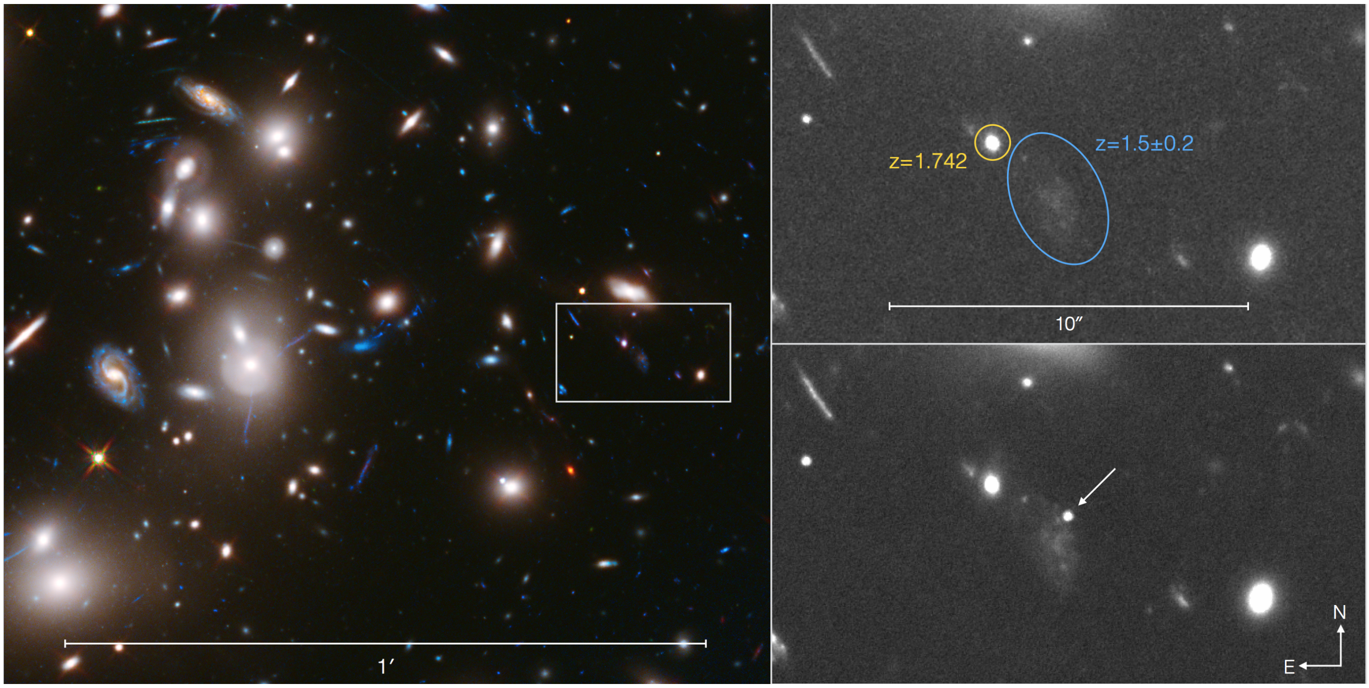

Figure 1. SN HFF14Tom in the Abell 2744 field. The left panel shows a UV/Optical/IR color composite image constructed from all available HST imaging of the Abell 2744 cluster field. The inset panels on the right show F814W imaging of the immediate vicinity of SN HFF14Tom, approximately 40″ from the center of the cluster. The top panel shows the template image, combining all data prior to the SN appearance. Labeled ellipses mark the nearest galaxies and their redshift constraints: a photometric redshift for the most likely host galaxy is marked in blue, and the spectroscopic redshift for a background galaxy is given in yellow. The bottom panel is constructed from all HFF F814W imaging taken while the SN was detectable, and marks the SN location with an arrow. (Left panel image credit: NASA, ESA, and J. Lotz, M. Mountain, A. Koekemoer, and the HFF Team (STScI))

discretionary initiative that is collecting 140 orbits of HST imaging (roughly 340 ksec) on six massive galaxy clusters, plus 6 accompanying parallel fields. Each field is observed in 3 optical bands (ACS F435W, F606W and F814W) and 4 infrared (IR) bands (WFC3-IR F105W, F125W, F140W, and F160W), although the optical and IR imaging campaigns are separated by ∼6 months. Abell 2744 was the first cluster observed, with IR imaging spanning 2013 October-November, and optical imaging from 2014 May-July. A composite image of the HFF data showing the SN is presented in Figure 1. The SN detection was made in difference images constructed using template imaging of Abell 2744 from HST+ACS observations taken in 2009 (PI:Dupke, HST-PID:11689).

The most probable host galaxy for SN HFF14Tom is a faint and diffuse galaxy immediately to the south-east of the SN location. With photometry of the host galaxy collected from the template images, we fit the spectral energy distribution (SED) using the *BPZ* code – a Bayesian photometric redshift estimator (Benítez 2000). The best-fit SED template match is shown in Figure 2. From the *BPZ* analysis, we found the host to be most likely an actively star-forming galaxy at a redshift of $z = 1.5 \pm 0.2$.

Another nearby bright galaxy to the East of the SN has a spectroscopic redshift of $z = 1.742$. This redshift was determined from a spectrum taken with the G141 grism of the HST WFC3-IR camera, collected as part of the Grism Lens Amplified Survey from Space (GLASS, PI:Treu, PID:13459, Treu ????). **As we will see in Sections 3 and 4, the SN data are inconsistent with that redshift, meaning that this nearby galaxy is a background object and therefore has no impact on the SN classification or luminosity measurement.**

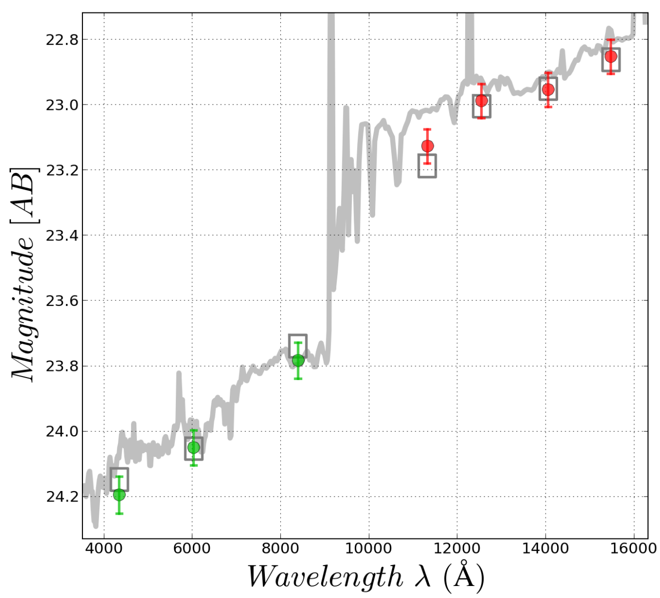

Figure 2. Best-fit SED template match for the most probable HFF14Tom host galaxy. Using the *BPZ* code to match the observed SED, we find the nearest galaxy to the SN position is a late type galaxy with a photometric redshift of $z = 1.5 \pm 0.2$.

Upon discovery, HST target-of-opportunity observations were triggered from the FrontierSN program (PI:Rodney, HST-PID:13386), which aims to discover and follow transient sources in the HFF cluster and paral-

Table 1
HFF14Tom Observations and Photometry

Obs. Date (MJD)	Camera	Filter or grism	Exp. Time (sec)	Flux (counts/sec)	Flux Err (counts/sec)	AB Mag[a]	Mag Err	AB Zero Point	ΔZP[b] (Vega-AB)
56820.06	ACS	F435W	5083	-0.027	0.053	27.66	...	25.665	-0.102
56821.85	ACS	F435W	5083	0.105	0.053	28.11	0.55	25.665	-0.102
56823.77	ACS	F435W	5083	0.022	0.053	29.80	2.59	25.665	-0.102
56824.97	ACS	F435W	5083	0.021	0.053	29.85	2.72	25.665	-0.102
56828.68	ACS	F435W	5083	-0.148	0.053	27.65	...	25.665	-0.102
56830.87	ACS	F435W	5083	0.100	0.054	28.16	0.58	25.665	-0.102
56832.86	ACS	F435W	5083	-0.080	0.053	27.66	...	25.665	-0.102
56833.86	ACS	F435W	5083	-0.002	0.053	27.67	...	25.665	-0.102
56839.50	ACS	F435W	5083	-0.022	0.052	27.68	...	25.665	-0.102
56792.06	ACS	F606W	5046	0.363	0.083	27.59	0.25	26.493	-0.086
56792.98	ACS	F606W	3586	0.692	0.095	26.89	0.15	26.493	-0.086
56797.10	ACS	F606W	4977	0.968	0.087	26.53	0.10	26.493	-0.086
56800.08	ACS	F606W	4977	0.844	0.085	26.68	0.11	26.493	-0.086
56804.99	ACS	F606W	5046	0.977	0.086	26.52	0.10	26.493	-0.086
56792.99	ACS	F814W	3652	1.639	0.104	25.41	0.07	25.947	-0.424
56797.11	ACS	F814W	4904	3.376	0.141	24.63	0.05	25.947	-0.424
56798.95	ACS	F814W	5046	3.951	0.156	24.46	0.04	25.947	-0.424
56800.10	ACS	F814W	4904	3.854	0.155	24.48	0.04	25.947	-0.424
56801.89	ACS	F814W	10092	4.102	0.153	24.41	0.04	25.947	-0.424
56802.95	ACS	F814W	10092	4.325	0.160	24.36	0.04	25.947	-0.424
56803.93	ACS	F814W	15138	4.402	0.160	24.34	0.04	25.947	-0.424
56804.08	ACS	F814W	5046	4.658	0.178	24.28	0.04	25.947	-0.424
56812.08	ACS	F814W	637	4.705	0.258	24.27	0.06	25.947	-0.424
56815.93	ACS	F814W	446	4.026	0.285	24.43	0.08	25.947	-0.424
56820.07	ACS	F814W	5044	3.508	0.142	24.58	0.04	25.947	-0.424
56821.87	ACS	F814W	5044	3.541	0.144	24.57	0.04	25.947	-0.424
56823.79	ACS	F814W	5044	2.876	0.124	24.80	0.05	25.947	-0.424
56824.99	ACS	F814W	5044	3.060	0.129	24.73	0.05	25.947	-0.424
56828.70	ACS	F814W	5044	2.777	0.121	24.84	0.05	25.947	-0.424
56830.89	ACS	F814W	5044	2.395	0.111	25.00	0.05	25.947	-0.424
56832.88	ACS	F814W	5044	2.331	0.108	25.03	0.05	25.947	-0.424
56833.88	ACS	F814W	5044	2.389	0.111	25.00	0.05	25.947	-0.424
56839.52	ACS	F814W	5044	1.673	0.093	25.39	0.06	25.947	-0.424
56833.14	WFC3-IR	F105W	756	7.504	0.239	24.08	0.03	26.269	-0.645
56841.82	WFC3-IR	F105W	756	5.822	0.208	24.36	0.04	26.269	-0.645
56850.06	WFC3-IR	F105W	756	3.952	0.207	24.78	0.06	26.269	-0.645
56860.62	WFC3-IR	F105W	1159	2.899	0.167	25.11	0.06	26.269	-0.645
56886.63	WFC3-IR	F105W	1159	1.216	0.147	26.06	0.13	26.269	-0.645
56891.67	WFC3-IR	F105W	356	0.971	0.324	26.30	0.36	26.269	-0.645
56893.20	WFC3-IR	F105W	712	0.954	0.242	26.32	0.28	26.269	-0.645
56954.64	WFC3-IR	F105W	356	0.521	0.388	26.98	0.81	26.269	-0.645
56817.08	WFC3-IR	F125W	1206	8.459	0.191	23.91	0.02	26.230	-0.901
56833.15	WFC3-IR	F125W	756	7.753	0.255	24.01	0.04	26.230	-0.901
56841.83	WFC3-IR	F125W	806	6.015	0.227	24.28	0.04	26.230	-0.901
56850.07	WFC3-IR	F125W	806	4.343	0.224	24.64	0.06	26.230	-0.901
56891.86	WFC3-IR	F140W	712	2.578	0.344	25.42	0.14	26.452	-1.076
56893.06	WFC3-IR	F140W	712	3.026	0.363	25.25	0.13	26.452	-1.076
56955.58	WFC3-IR	F140W	1424	1.218	0.269	26.24	0.24	26.452	-1.076
56817.09	WFC3-IR	F160W	1206	4.831	0.263	24.24	0.06	25.946	-1.251
56833.21	WFC3-IR	F160W	756	3.965	0.241	24.45	0.07	25.946	-1.251
56841.84	WFC3-IR	F160W	756	3.011	0.234	24.75	0.08	25.946	-1.251
56850.08	WFC3-IR	F160W	756	2.744	0.223	24.85	0.09	25.946	-1.251
56860.67	WFC3-IR	F160W	1159	1.895	0.177	25.25	0.10	25.946	-1.251
56886.64	WFC3-IR	F160W	1159	1.677	0.191	25.38	0.12	25.946	-1.251
56812.0	ACS	G800L	3490	...	...	...	...	...	...
56815.7	ACS	G800L	6086	...	...	...	...	...	...

[a] For non-positive flux values we report the magnitude as a 3-σ upper limit
[b] Zero point difference: the magnitude shift for conversion from AB to Vega magnitude units.

lel fields. The FrontierSN observations provided WFC3-IR imaging as well as spectroscopy using the ACS G800L grism, supplementing the rapid-cadence optical imaging from HST+ACS already being provided by the HFF program. **The last detections in the IR F105W and F140W bands came from the direct-imaging component of the GLASS program**. Difference images for the IR follow-up data were generated using templates constructed from the HFF WFC3-IR imaging campaign, which concluded in November, 2013.

All of the imaging data were processed using the `sndrizpipe` pipeline,[4] a custom data reduction package in Python that is employs the `DrizzlePac` tools from

[4] `https://github.com/srodney/sndrizpipe` v1.2 DOI:10.5281/zenodo.10731

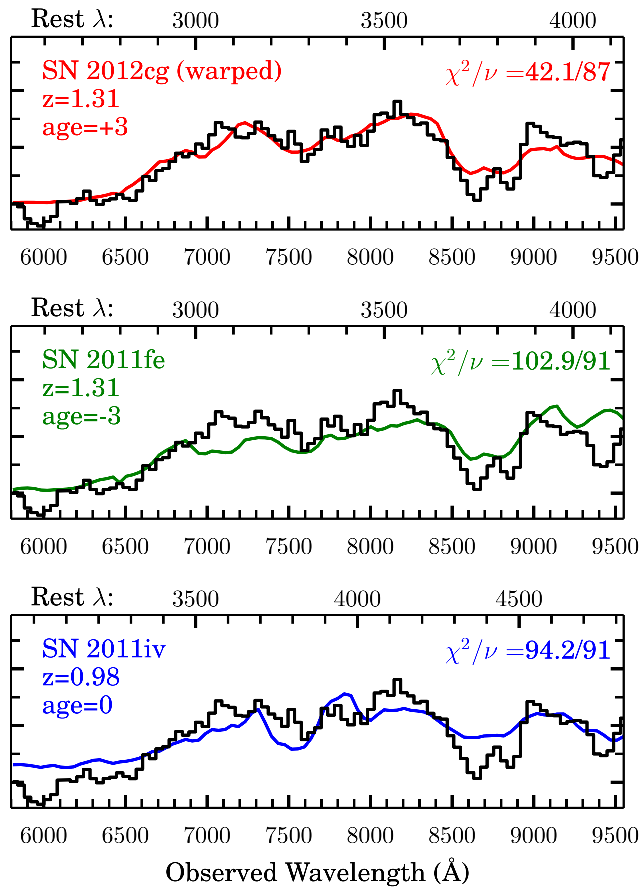

Figure 3. Redshift and age determination from spectral template matching to the the SN HFF14Tom maximum light spectrum. The y axis plots flux in arbitrary units, and the x axis marks wavelength in Å with the observer-frame on the bottom and rest-frame on the top. The HFF14Tom spectrum observed with the HST ACS G800L grism is shown in black, overlaid with model fits derived from a library of Type Ia templates that have extended rest-frame UV coverage. *Top*: The best match is at $z = 1.31$ with age=+3 days, from the normal Type Ia SN 2012cg template when using a smooth 3rd-order polynomial to warp the shape of the template pseudo-continuum. When the templates are not warped, an acceptable fit can be found with a normal Type Ia at $z = 1.31$ (middle) or at $z \sim 1$ (bottom), although the latter is inconsistent with the host galaxy redshift prior and the light curve. No CC SN templates can provide a statistically acceptable fit at any redshift, within the age constraints imposed by the light curve.

the Space Telescope Science Institute (STScI) (Fruchter et al. 2010). Photometry was collected using the `PyPhot` software package,[5] a pure-Python implementation of the photometry algorithms from the IDL AstroLib package (Landsman 1993), which in turn are based on the DAOPHOT program (Stetson 1987). For the IR bands we used point spread function (PSF) fitting on the difference images, and in the ACS optical bands we collected photometry with a $0\farcs3$ aperture. Table 1 presents the list of observations, along with measured photometry from all available imaging data.

3. SPECTROSCOPY

A spectrum of SN HFF14Tom was collected with the ACS G800L grism on 2014 June 4 and 7, when the SN was very near to its peak brightness. The observations – listed at the bottom of Table 1 – used 5 HST orbits from the FrontierSN program for a total spectroscopic exposure time of ∼10 ksec. The grism data were processed and the target spectrum was extracted using a custom pipeline (Brammer et al. 2012), which was developed for the 3D-HST program (PI:Van Dokkum; PID:12177, 12328) and also used by the Grism Lens Amplified Survey from Space (GLASS; PI:Treu; PID:13459).

Figure 3 shows the composite 1-D ACS grism spectrum, combining all available G800L exposures, overlaid with SN model fits that will be described below. The spectrum is largely free of contamination, because the orientation was chosen to avoid nearby bright sources and the host galaxy is diffuse and optically faint. Thus, the SN spectral features can be unambiguously identified, most notably the red slope of the continuum and a prominent absorption feature at ∼8700Å. However, the signal to noise ratio (S/N) for the host galaxy spectrum was too weak to yield any additional constraints on the host type or redshift.

As described below, we fit the SN HFF14Tom spectrum in two steps. First we determine a spectral classification – and get a preliminary estimate of the redshift and age – using the SuperNova IDentification (SNID) software (Blondin & Tonry 2007). Second, we refine the redshift and age measurement using a custom Type Ia spectral template matching program.

3.1. *Classification with SNID*

The SNID program is designed to estimate the type, redshift, and age of a SN spectrum through cross-correlation matching with a library of template spectra, **using the algorithm of Tonry & Davis (1979).** To account for possible distortions in the broad shape of the SN pseudo-continuum due to dust or instrumental calibration effects, SNID divides each SED by a smooth cubic spline fit. This effectively removes the shape of the SN pseudo-continuum to leave behind a flat SED superimposed with spectral absorption and emission features. It is these features which drive the cross-correlation fit, so the SNID approach is insensitive to the overall color of the SED. We used v2.0 of the SNID template library, which includes template SEDs covering all Type Ia and Core Collapse sub-classes, and has recently been updated with corrections and improvements to the Type Ib/c templates (Liu & Modjaz 2014).

In SNID the goodness of fit is evaluated primarily through the *rlap* parameter, which measures the degree of wavelength overlap and the strength of the cross-correlation peak. Typically, an *rlap* value > 5 is required to be considered an acceptable match.

To match the SN HFF14Tom spectrum we use conservative constraints on age and redshift: limiting the age to ±5 rest-frame days of peak brightness and $0.8 < z < 1.8$, consistent with the SN light curve and host galaxy photo-z. With these constraints we find that the only acceptable match is a normal Type Ia SN near $z = 1.3$. The best match has *rlap*$= 8.7$, using the normal Type Ia SN 2005cf at $z = 1.35$ and age=-2.2 rest-frame days before peak. Within these constraints, the best non-Ia matches all have *rlap*< 2.5.

[5] `https://github.com/djones1040/PyPhot`

Using SNID we can find an acceptable CC SN match only when we remove all age and redshift constraints. In this case the best non-Ia match is the Type Ic SN 1997ef, which delivers *rlap*= 6.8 at $z = 0.51$ and age=47.3 rest-frame days past peak. This is not as good a fit as the best Type Ia models, is at odds with the host galaxy redshift prior, and is strongly disfavored by the shape and colors of the SN light curve (see Section 4).

From the preceding analysis, we conclude that HFF14Tom is a Type Ia SN at $z \approx 1.3$. At this redshift, the absorption at ∼8700Å corresponds to the blended Ca II H&K features. This Ca II absorption is commonly seen in Type Ia SN spectra near maximum light, although it is also prominent in the spectra of Type Ib and Ic core collapse SNe (CC SNe). The red color of the HFF14Tom SED is qualitatively consistent with a redshift of $z > 1$ – although this information was not used by SNID for the template matching. As we will see in Section 4, this spectral classification of SN HFF14Tom is reinforced by the photometric information, which also supports classification as a Type Ia SN at $z \approx 1.3$.

3.2. *Spectroscopic Redshift*

To refine the redshift and phase constraints on HFF14Tom, we next fit the spectrum with a custom spectral matching program that employs a library of Type Ia SN SEDs. This library is similar to the Type Ia spectral set used by SNID, but also includes more recent SNe with well-observed spectral time series that extend to rest-frame UV wavelengths (e.g. SN 2011fe and 2014J). We first use an approach similar to the SNID algorithm: warping the pseudo-continuum of each template spectrum by dividing out a 3rd-order polynomial to match the observed SED of SN HFF14Tom. From this analysis we find results that are consistent with the SNID fits: a redshift of $z = 1.31 \pm 0.01$ and a phase of 0 ± 3 rest-frame days. The best-fitting spectral template is the normal Type Ia SN 2012cg, shown in the bottom panel of Figure 3, which has χ^2 per degree of freedom ν equal to 42.1/87.

Finally, we repeat the fitting, but without any warping of the templates to account for differences in the continuum shape. In this iteration we only allow each template SED to be scaled in flux coherently at all wavelengths. As shown in Figure 3, we again find that the HFF14Tom SED can be matched by a normal Type Ia SN (SN 2011fe) at redshift $z = 1.31 \pm 0.01$. Without the continuum warping, an alternative fit also arises: the normal Type Ia SN 2011iv at $z = 0.98 \pm 0.01$. Formally, this match provides a slightly better fit to the unwarped HFF14Tom spectrum, although the fit is notably poor at ~ 8700Å where the most significant absorption feature is found. Furthermore, a redshift $z \sim 1$ is at odds with the host galaxy photo-z (1.5 ± 0.2), and we will see in the following section that the photometric data is incompatible with a normal Type Ia SN at $z \sim 1.0$.

Setting aside the $z \sim 1$ solution, all other template matches provide a consistent redshift constraint of $z = 1.31 \pm 0.01$, regardless of whether the templates are warped to match the SN HFF14Tom continuum shape. The inferred age from these fits is 0 ± 3 rest-frame days from peak brightness, which is also consistent with the observed light curve.

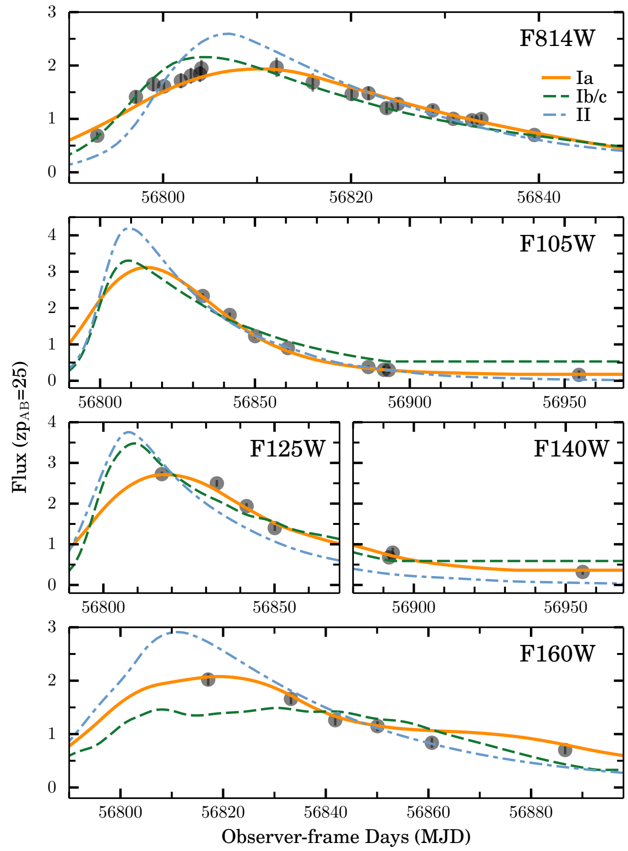

Figure 4. Maximum likelihood model for each SN sub-class, derived from Bayesian model selection using the photometric data alone. Grey points show the observed SN HFF14Tom photometry with error bars, though these are typically smaller than the size of the marker. The Type Ia model (orange solid line) is drawn from the SALT2 template at $z = 1.35$. The best match from all Type Ib/Ic models is based on the Type Ic SN SDSS-14475 at $z = 0.695$ (green dashed line). For the Type II class, the best match is from the Type II-L SN 2007pg at $z = 1.8$ (blue dash-dot line). The Type Ia model is by far the best match, and the only one that is consistent with both the photo-z of the probable host galaxy and the spectroscopic redshift from the SN spectrum.

4. PHOTOMETRIC CLASSIFICATION

Relative to other SNe at $z > 1$, the SN HFF14Tom light curve was unusually well sampled at rest-frame ultraviolet wavelengths, due to the rapid cadence of the HFF imaging campaign. These ACS observations therefore provide a tight constraint on the time of peak brightness and the evolution of the SN color. Supplemental observations with the WFC3-IR camera provided critical rest-frame optical photometry, enabling a measurement of the apparent luminosity distance through light curve fitting.

As a check on the spectral classification of SN HFF14Tom (Section 3.1), we independently classified the SN using a Bayesian photometric classifier. We use the sncosmo software package[6] to simulate SN light curves from $z = 0.3$ to 2.3 and evaluate the classification probability using traditional Bayesian model selection (as in Jones et al. 2013; Rodney et al. 2014; Graur et al. 2014; ?). In this analysis we represent normal Type Ia SNe

[6] http://sncosmo.github.io/

with the SALT2 model (Guy et al. 2010), and CC SNe with 42 discrete templates (26 Type II and 16 Type Ib/c) drawn from the template library of the SuperNova Analysis software package (SNANA, Kessler et al. 2009b).[7] Likelihoods are defined by comparing the observed fluxes to model predictions in all passbands where the model is defined. In practice, this means we exclude the F435W and F606W bands, which are too blue for our models at $z > 0.85$.

The CC SN models have free parameters for date of peak brightness ($t_{\rm pk}$), amplitude, and redshift (z). Due to the expected impact of gravitational lensing magnification, we do not include any prior on the intrinsic luminosity for any SN sub-class. We also do not assign a prior for the SN redshift. This allows our photometric analysis to provide an independent check on the host galaxy photo-z and spectroscopic redshift (Sections 2 and 3.2).

For Type Ia SNe, the SALT2 model has two additional parameters that control the shape (x_1) and color (c) of the light curve. We use conservative priors here, defined to encompass a range of Type Ia SN shapes and colors that is broader than typically allowed in cosmological analyses (see e.g., Kessler et al. 2009a; Sullivan et al. 2011; Rest et al. 2014). For x_1 the prior is a bifurcated Gaussian distribution with mean $\bar{x}_1 = 0$, dispersion $\sigma^+_{x_1} = 0.9$ and $\sigma^-_{x_1} = -1.5$. The prior for the color parameter c has $\bar{c} = 0.0$, $\sigma^-_c = 0.08$, and $\sigma^+_c = 0.54$. The c parameter in SALT2 combines intrinsic SN color and extinction due to dust, so the large red tail of this distribution allows for the possibility of several magnitudes of dust extinction along the HFF14Tom line of sight.

We also assign a class prior for each of the three primary SN sub-classes (Type Ia, Ib/c, and II), using a fixed relative fraction for each sub-class as determined at $z = 0$ by Smartt et al. (2009) and Li et al. (2011). A more rigorous classification would extrapolate these local SN class fractions to higher redshift using models or measurements of the volumetric SN rate. For simplicity, we do not vary the class priors with redshift, and in practice these priors do not have any significant impact on the resulting classification.

The final photometric classification probability for SN HFF14Tom is $p(\mathrm{Ia}|\mathbf{D}) = 1.0$, with the classification probability from all CC SN sub-classes totaling less than 10^{-32}. **Although this Bayesian classification utilizes the full posterior probability distribution, for illustration we highlight in Figure 4 a single best-fit model for each sub-class.** This demonstrates how the CC SN models fail to adequately match the observed photometry. In particular, only the Type Ia model can simultaneously provide an acceptable fit to the well-sampled rising light curve in F814W and the F814W-F160W color near peak.

The marginal posterior distribution in redshift for the Type Ia model is sharply peaked at $z = 1.35 \pm 0.02$, which is fully consistent with the photo-z of the presumed host galaxy ($z = 1.5 \pm 0.2$), and $< 2\sigma$ from the spectroscopic redshift of $z = 1.31 \pm 0.01$ derived in Section 3.2. The time of peak brightness is also tightly constrained at $t_{\rm pk} = 56816.3 \pm 0.3$, which means the spectroscopic observations were collected within 2 rest-frame days of the epoch of peak brightness, consistent with our spectroscopic analysis.

[7] Throughout this work we use SNANA v10_35g.

Table 2
HFF14Tom Measured Magnification

Fitter	Distance Modulus HFF14Tom	Distance Modulus Control	Measured Magnification
MLCS2k2	44.06 ± 0.09	44.81 ± 0.05	2.00 ± 0.19
SALT2	44.09 ± 0.16	44.78 ± 0.05	1.89 ± 0.29

5. LIGHT CURVE FITTING

With the spectroscopic type and redshift securely defined as a normal Type Ia SN at $z = 1.31$, we now turn to fitting the light curve with Type Ia templates to measure the distance modulus. Here we use two independent light curve fitters: the SALT2 model described above and the MLCS2k2 model (Jha et al. 2007).

With both fitters we find light curve shape and color parameters that are fully consistent with a normal Type Ia SN, regardless of whether we adopt the spectroscopic redshift $z = 1.31$ from Section 3.2 or the photometric redshift $z = 1.35$ from Section 4. For SALT2, with the redshift range set to 1.33 ± 0.02, we find a light curve shape parameter of $x_1 = 0.164 \pm 0.199$ and a color parameter of $c = -0.115 \pm 0.025$, yielding a χ^2 value of 48.4 for 36 degrees of freedom, ν. With the MLCS2k2 fitter the best-fit shape parameter is $\Delta = -0.033 \pm 0.083$ and the color term is $A_{\rm V} = 0.014 \pm 0.037$, giving $\chi^2/\nu = 23.9/36$.

5.1. *Distance Modulus*

As in P14, we derive a distance modulus[8] from the SALT2 fit using

$$\mathrm{dm}_{\rm SALT2} = m^*_B - M + \alpha(s-1) - \beta C. \quad (1)$$

Here the parameters for light curve shape s and color C correspond to the SiFTO light curve fitter (Conley et al. 2008), so we first use the formulae from Guy et al. (2010) to convert from SALT2 (x_1 and c) into the equivalent SiFTO parameters. We also add an offset of 0.27 mag to the value of m^*_B returned by SNANA, in order to match the arbitrary normalization of the SALT2 fitter used by Guy et al. (2010) and Sullivan et al. (2011). This conversion allows us to adopt values for the constants M, α, and β from Sullivan et al. (2011), which have been calibrated using 472 SNe from the SNLS3 sample (Conley et al. 2011): $M = -19.12 \pm 0.03$, $\alpha = 1.367 \pm 0.086$, and $\beta = 3.179 \pm 0.101$.

The SNANA version of the MLCS2k2 fitter returns a value for the distance modulus ($\mathrm{dm}_{\rm MLCS2k2}$) that has an arbitrary zero point offset relative to the SALT2 distances ($\mathrm{dm}_{\rm SALT2}$). To put the two distances onto the same reference frame we add a zeropoint correction of 0.20 mag to the MLCS2k2 distances as in P14. This correction was derived by applying both fitters to a sample of Type Ia SNe from the SDSS survey (Holtzman et al. 2008; Kessler et al. 2009a), with the extinction law R_V fixed at 1.9.

Final values for the SN distance modulus are shown in Table 2, both for the spectroscopic redshift ($z = 1.31$)

[8] We use 'dm' to indicate the distance modulus to avoid confusion, reserving the symbol μ to refer to the lensing magnification. This 'dm' is a standard distance modulus, defined as $\mathrm{dm} = 5\log_{10} d_L + 25$, where d_L is the luminosity distance in Mpc.

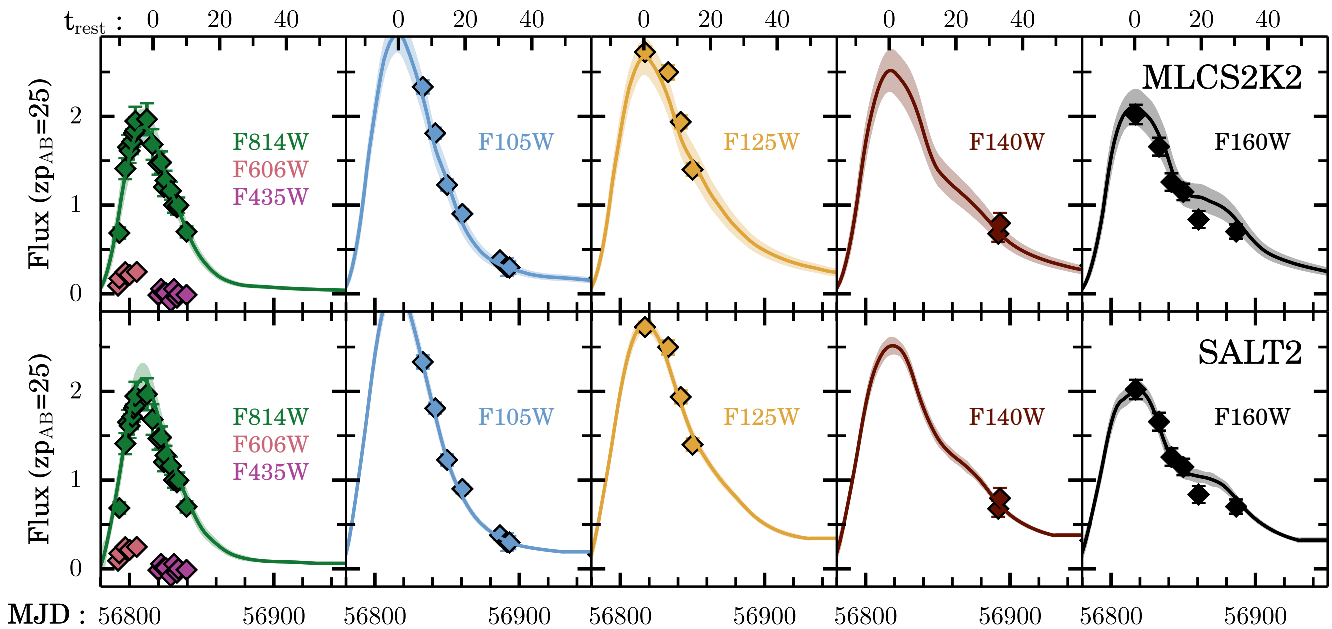

Figure 5. Type Ia light curve fits to SN HFF14Tom using the MLCS2k2 (top row) and SALT2 (bottom row) fitters. The model redshifts are set to $z = 1.33 \pm 0.02$, encompassing both redshift values as determined from spectroscopic and photometric constraints. Solid lines denote the best-fit model and shaded lines show the range allowed by 1-σ uncertainties on the model parameters. Observed fluxes are shown as diamonds, scaled to an AB magnitude zero point of 25. Error bars are plotted, but most are commensurate with the size of the points. The left-most panel includes observations in the F435W and F606W filters, although these were not used for the fit, as they are bluer than the minimum wavelength for the model. The lower axis marks time in observer frame days, while the top axis shows the time in the rest frame relative to the epoch of peak brightness.

and the photometric redshift ($z = 1.35$). The two light curve fitters are consistent within the uncertainties.

5.2. *Magnification*

To measure the lensing magnification, we would like to avoid introducing systematic uncertainties inherent to any assumed cosmological model (e.g. Nordin et al. 2014). To that end, we follow P14 and define the magnification by comparing the measured distance modulus of SN HFF14Tom against an average distance modulus derived from a “control sample” of unlensed Type Ia SN at similar redshift. This allows us to make only the minimal assumption that the redshift-distance relationship for Type Ia SN is smooth and approximately linear over a small redshift span, which should be true for any plausible cosmological model.

The unlensed sample comprises 18 spectroscopically confirmed Type Ia SNe in the range $1.14 \leq z \leq 1.42$ from the GOODS and SCP surveys,[9] which used the HST Advanced Camera for Surveys (Riess & Livio 2006; Suzuki et al. 2012). Using the SALT2 and MLCS2k2 fitters as described above, we get distance modulus measures for every object in this control sample. We then fit a linear relationship for distance modulus vs. redshift, and derive a prediction for the distance modulus of a normal Type Ia SN at the redshift of SN HFF14Tom(Figure 6). This predicted value is given in Table 2 under the “Control” column. The difference between the observed distance of SN HFF14Tom and this control sample value is attributed to the magnification from gravitational lensing:

$$\mathrm{dm}_{\mathrm{control}} - \mathrm{dm}_{\mathrm{HFF14Tom}} = 2.5 \log_{10} \mu. \qquad (2)$$

This inferred magnification is reported in the final column of Table 2.

6. DISCUSSION

6.1. *Comparison to Model Predictions*

Before the Frontier Fields observations began, the Space Telescope Science Institute (STScI) issued a call for lens modeling teams to generate mass models of all 6 Frontier Field clusters, using a shared collection of all imaging and spectroscopic data available at the time. In response to this opportunity, five teams generated eight models for Abell 2744. **These models necessarily relied on pre-HFF data, and were required to be complete before the HFF program began, in order to enable the estimation of magnifications for any new lensed background sources revealed by the HFF imaging.** An interactive web tool was created by D. Coe and hosted at STScI, to extract magnification estimates and uncertainties from each model for any given redshift and position. In this work we also consider three additional models that were created later, taking advantage of new multiply-imaged galaxies discovered in the HFF imaging as well as new redshifts for lensed background galaxies.

Table 3 lists the 11 models, giving for each one the predicted magnification and uncertainty for a source at $z = 1.31 \pm 0.01$ and at the position of HFF14Tom. These

[9] GOODS: Great Observatories Origins Deep Survey, PI:Giavalisco, HST-PID:9425,9583; SCP: Supernova Cosmology Project, PI:Perlmutter

Table 3
Predicted magnifications for SN HFF14Tom from lens models.

Model	Best [a]	Median[b]	References	Description
Sharon(v2)	2.73	$2.69^{+0.14}_{-0.06}$	Jullo et al. 2007;Johnson et al. 2014	LENSTOOL parametric, strong-lensing based model
CATS-SL	2.25	$2.27^{+0.05}_{-0.04}$	Jullo & Kneib 2009; Jauzac et al. 2012	LENSTOOL hybrid parametric/free-form, strong lensing based model.
CATS-SL+WL	...	$2.62^{+0.18}_{-0.18}$	Jullo & Kneib 2009; Jauzac et al. 2012	LENSTOOL hybrid parametric/free-form, strong+weak lensing based model.
Jauzac	...	$3.37^{+0.14}_{-0.15}$	Jauzac et al. 2014a; Richard et al. 2014	Updated version of the CATS-SL model, adds 33 new multiply-imaged galaxies.
GLAFIC	2.32	$2.28^{+0.07}_{-0.11}$	Oguri 2010; Ishigaki et al. 2015	Parametric strong-lensing model using the `GLAFIC` code.[d]
Zitrin-NFW	2.07	$2.27^{+0.23}_{-0.22}$	Zitrin et al. 2009	Parametric strong-lensing model using PIEMD[e] profiles for galaxies and NFW[f] profiles for dark matter halos.
Zitrin-LTM	2.64	$2.96^{+0.77}_{-0.38}$	Zitrin et al. 2013	Parametric strong-lensing model, adopts the Light-Traces-Mass assumption for both the luminous and dark matter.
Bradac(v1)	3.15	$2.45^{+0.19}_{-0.16}$	Bradač et al. 2005, 2009	`SWUnited` : Free-form, strong+weak-lensing based model
Bradac(v2)	2.23	$2.20^{+0.03}_{-0.01}$	Bradač et al. 2005, 2009	**Updated version of the `SWUnited` model with new strong-lensing constraints from HFF imaging.**
Williams	2.67	$2.78^{+2.68}_{-1.14}$	Liesenborgs et al. 2006; Mohammed et al. 2014	`GRALE`[g] : Free-form strong-lensing model using a genetic algorithm.
Merten	2.31	$2.22^{+0.67}_{-0.19}$	Merten et al. 2009, 2011	`SaWLENS`,[h] Grid-based free-form strong+weak lensing based model using adaptive mesh refinement.
Lam	...	$2.77^{+0.36}_{-0.36}$	Sendra et al. 2014; Lam et al. 2014	`WSLAP+`[h] : Free-form model strong-lensing using a grid-based method, supplemented by deflections fixed to cluster member galaxies.
Diego[i]	...	$2.10^{+0.36}_{-0.36}$	Sendra et al. 2014; Lam et al. 2014	**Alternative implementation of the `WSLAP+`[h] model, using a different set of strong-lensing constraints and redshifts.**

[a] The magnification returned for the optimal version of each model, as independently defined by each lens modeling team.
[b] Median magnification from 100-600 Monte Carlo realizations of the model. Uncertainties enclose 68% of the realized values.
[c] `LENSTOOL` : `http://projects.lam.fr/repos/lenstool/wiki`
[d] `GLAFIC` : `http://www.slac.stanford.edu/~oguri/glafic/`
[e] PIEMD: Pseudo Isothermal Elliptical Mass Distrubution
[f] NFW : Navarro-Frenk-White mass density profile (Navarro et al. 1997).
[g] `GRALE` :
[h] `SaWLENS` : Strong and Weak LENSing analysis code. `http://www.julianmerten.net/codes.html`
[h] `WSLAP+` : Weak and Strong Lensing Analysis Package plus member galaxies **(Note: no weak-lensing constraints used for Abell 2744)**
[i] **No uncertainty estimates were available for the Diego implementation of the `WSLAP+` model, so we adopt the uncertainties from the Lam model.**

models represent a broad sampling of the techniques and assumptions that can be applied to the modeling of mass distributions in galaxy clusters. A rigorous comparison of these disparate lens modeling techniques is beyond the scope of this work. Table 3 includes a brief description of each model, but for a complete discussion of the methodology the reader is referred to the listed references.

In Figure 7 the model predictions are plotted alongside the observed magnification of SN HFF14Tom, derived in Section 5.2. This comparison shows that these 11 models are largely consistent with each other. Naively treating each model as an independent prediction for the magnification (and ignoring their quoted uncertainties), one would get a mean for the full sample of $\mu = 2.62 \pm 0.34$ (shown as a grey band in Figure 7). This is separated from the observed SN magnification by $\delta\mu/\mu = 30\%$, which is a 1.7σ difference.

The models shown in Figure 7 are separated along the y direction into two broad classes, with the six **so-called** *parametrized* models on top and the four *free-form* models on the bottom.[10] Broadly speaking, the parametric models use parameterized density distributions to describe the arrangement of mass within the cluster, typically associating massive dark matter halos with the positions of bright cluster member galaxies. Therefore, parametric models rely (to varying degrees) on the assumption that the observed light from cluster galaxies is a good tracer of the cluster's dark matter. Free-form models divide the cluster into a grid, generally using an

[10] **Although this nomenclature is becoming standard in the literature, it is somewhat misleading, as the pixels or grid cells in free-form models are effectively parameters as well. Perhaps "simply-parameterized" would be more accurate, though we adopt the more common usage here.**

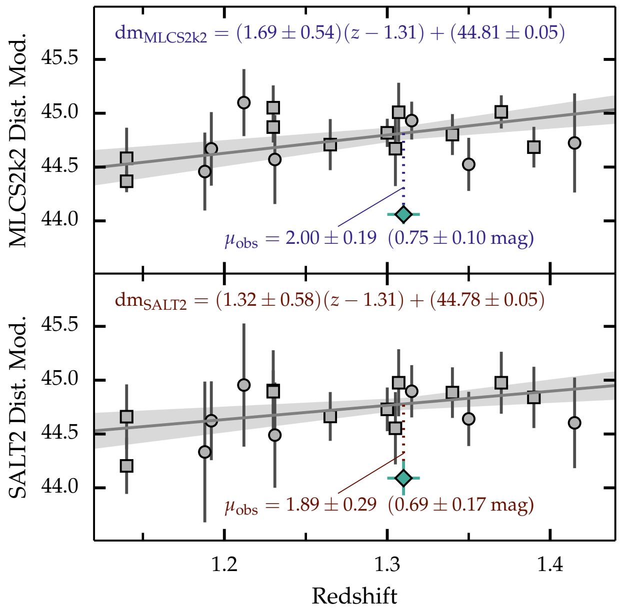

Figure 6. Measurement of the lensing magnification from comparison of the HFF14Tom distance modulus to a sample of unlensed field SN. The distance modulus for each SN is derived from light curve fits using the MLCS2k2 fitter (top panel) and the SALT2 fitter (bottom panel).

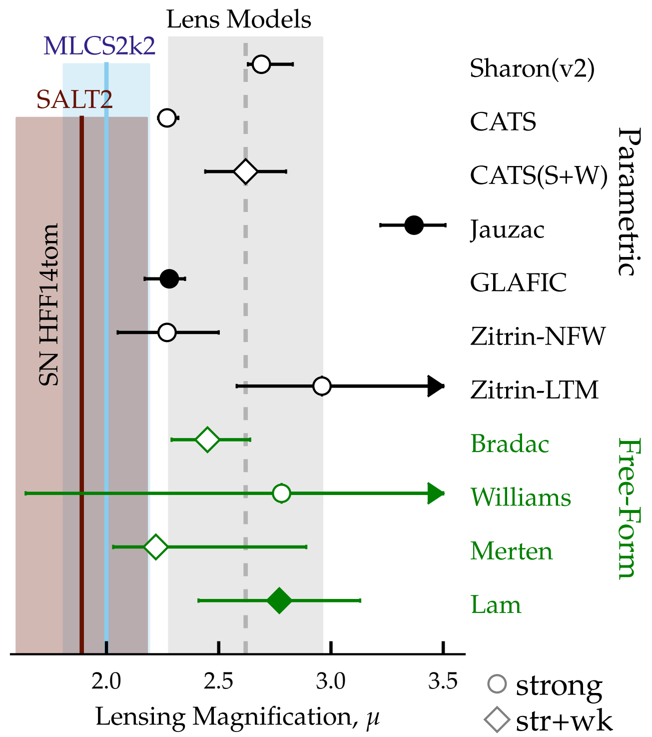

Figure 7. Comparison of the observed lensing magnification to predictions from lens models. Solid vertical lines show the constraints from SN HFF14Tom derived in Section 5.2 using the SALT2 (red) and MLCS2k2 (blue) fitters, with shaded regions marking the total uncertainty for each. Markers with horizontal error bars show the median magnification and 68% confidence region from each of the 10 lensing models. Circles indicate models that use only strong-lensing constraints, while diamonds denote those that also incorporate weak-lensing measurements. Models shown with open markers were constructed using only data available before the start of the Frontier Fields observations. Filled markers indicate models that use additional input constraints, including new multiply imaged systems and redshifts. The seven models shown in black at the top are from the "parametric" family, and the four in green at the bottom are "free-form." The dashed grey line marks the unweighted mean of all model magnifications, with grey shading indicating the standard error of the mean from naively assuming all are independent predictions.

adaptive mesh to get better sampling in denser regions. Each grid cell is assigned a mass or a potential, and then the grid spacing and the mass values are iteratively refined to match the observed lensing constraints.

Figure 7 also separates the models based on the scope of input data constraints used. Seven of the models rely only on strong-lensing constraints (plotted as circles), while the other four also use weak-lensing measurements (diamonds). Eight of the models were constructed using only pre-HFF data (open symbols), and three others added new multiply-imaged systems and redshifts.

In spite of the great variety in input data and methodology, these lens models overall are delivering consistent and fairly accurate estimates of the magnification. **Four of the tested models (CATS, GLAFIC, Zitrin-NFW, Merten) report a median value that falls within the 1σ uncertainty range of the measured magnification, and two of the models (Williams, Merten) report uncertainties that overlap the central μ from at least one of the light curve fitters.** Furthermore, the scatter amongst models provides a reasonable estimate of the magnification uncertainty.

This is largely in agreement with the results of P14 and Nordin et al. (2014). The fact that the model predictions are collectively within 2σ of the observed magnification is especially encouraging for these Abell 2744 models. This is a merging cluster with a complex mass distribution, and most of the models we are evaluating are preliminary products, generated quickly and without access to the rich data from the Frontier Fields program.

However, beyond this first-order agreement, there is a systematic bias apparent. All of the lens models predict a magnification that is *higher* than the observed value, and no model has a median value that falls within the 1σ range of the observed magnifications. It is important to emphasize that SN HFF14Tom only samples a single sight-line through the cluster, so any conclusions to be drawn from this analysis are necesssarily limited. Nevertheless, a systematic shift common to all models is surprising, given the wide range of modeling strategies, input data, and physical assumptions represented by this set of models. In the following subsections we examine possible explanations for this apparently universal bias.

6.2. *Nearby Cluster Member Galaxy*

The line of sight to SN HFF14Tom is 5$''$.8 from a bright cluster member galaxy, due North of the SN position (see Figure 1). If the mass-to-light ratio (M/L) for this galaxy were significantly different from the M/L for other cluster member galaxies, then its proximity to the SN sight-line could introduce a bias in the magnification. This bias might be particularly acute for models that make a strict "light traces mass" assumption, such as the Sharon, CATS, Jauzac, GLAFIC and Zitrin-LTM models.

We tested this hypothesis using the Jauzac model by allowing the mass of the nearby cluster member galaxy to vary as a free parameter in the model. We found that the change in the SN HFF14Tom magnification prediction was less than $\Delta\mu = 0.1$. This additional dispersion is already included in the uncertainties quoted for that model in Table 3 and Figure 7. Furthermore, an erroneous M/L value for the nearby cluster member galaxy could not explain the systematic shift of all lens models, because some do not incorporate cluster member galaxies into their constraints at all (the free-form Bradac, Williams and Merten models).

6.3. *Sparse Strong Lensing Constraints*

At the outset of the HFF survey, only 33 multiply-imaged galaxies behind Abell 2744 were known. One might expect that the addition of new lensing constraints from the HFF data would improve the model constraints and reduce the tension between the predicted and observed magnification. However, for both of the most recent models (Jauzac et al. 2014b; Lam et al. 2014) that include new strong-lensing constraints, the predicted magnification is still significantly higher than the observed value. Again the CATS model family provides a useful case study. The Jauzac model shares the same lens modeling software (LensTool), and the same primary methodology as the earlier CATS models. A key difference is that the Jauzac model incorporates many new multiply imaged galaxies and corrects a mis-identified multiply-imaged system near the SN HFF14Tom position. These improvements should in principle make the Jauzac model magnification estimates more accurate, though we in fact see the opposite result: the Jauzac model predicts a μ that is higher than the measured value by 5.6σ.

This shift to higher magnifications is not, however, unique to the SN HFF14Tom position. Jauzac et al. (2014b) noted that their updated mass model of Abell 2744 results in a systematic increase in the magnification values across the cluster field. Examining a sample of ∼30 multiple images, Jauzac et al. found that the magnifications increased by a factor of ~ 1.5 relative to pre-HFF models. Although this single sight-line can only provide a very limited test of the model, the 5.6σ discrepancy is at least a strong suggestion that improving the number and quality of strong-lensing constraints can still lead to magnification maps that are susceptible to systematic biases.

6.4. ***Misidentification of System 3***

It is important to note that in regards to the impact on this particular sight-line, not all strong-lensing constraints are equal. An error in the association of multiple images or in the redshift of a multiply-imaged galaxy would have a more significant impact if that system has a projected position close to our SN sight-line. It happens that there is one such system, for which the position of a multiple image near SN HFF14Tom is presently disputed.

This multiply-imaged galaxy was originally labeled as *System 3* in Merten et al. (2011). As shown in Figure ??, it is stretched into two adjacent arcs northwest of the cluster core (images 3.1 and 3.2), with a third image on the western edge of the strong-lensing region (image 3.3 at 00:14:18.595, -30:23:58.42). Richard et al. (2014) echoed this initial identification in producing the `CATS` models, which we cite in Table 3 and Figure 7. In developing the `Sharon-v2` models, Johnson et al. (2014) provided a secure spectroscopic constraint of $z = 3.98 \pm 0.02$ for this system, based on a spectrum of the combined 3.1+3.2 source. The identification of the original image 3.3 has been called into question by two independent analyses. Using HFF imaging data, Lam et al. (2014) suggested an alternative third image for this system roughly 8″ to the south, which we will call $3.3'$ (00:14:18.39, -30:24:06.53). However, Lam et al. rejected this possibility based on a difference in colors between $3.3'$ and images 3.1 and 3.2. In contrast, Jauzac et al. argue that the position $3.3'$ is correct, and find that reassigning this multiple image results in a tighter model reconstruction for the locations of other multiply-imaged systems in the vicinity.

Resolving the identification of this single multiply-imaged galaxy could be an important component in resolving the magnification discrepancy, though it is unlikely to completely remove the tension. It is true that the model that reassigns the position to $3.3'$ (`Jauzac`) is also the one with the largest deviation from our observed μ value. However, the bias is still present even if we remove that model and only consider models using the original position 3.3.

6.5. *Mass Profile Truncation*

Eight of the mass models evaluated here are constrained only using strong-lensing features such as multiply-imaged background galaxies and highly magnified arcs. There are now ∼150 known lensed images behind Abell 2744 (Jauzac et al. 2014b), but SN HFF14Tom is located several arcseconds outside the core region of the cluster where these multiply-imaged galaxies are found. Therefore these seven "strong-lensing only" models must necessarily rely on extrapolations to provide a prediction for the SN HFF14Tom magnification. If the true cluster density profile for Abell 2744 happens to be truncated – with a sharp drop right at the edge of this core strong-lensing region – then these seven models might well overestimate the mass interior to the HFF14Tom position, and thus systematically overestimate the magnification.

The other three models in our comparison set also use the strong lensing constraints from the core region, but additionally utilize weak lensing measurements to provide additional constraints on the mass distribution farther from the cluster core. The signal from weak lensing relies on a large sample of background galaxies, so this constraint operates principally at separations more than 1′from the cluster core. At a projected separation of $\sim 40''$, SN HFF14Tom falls in between the strong- and weak-lensing regimes, and one would expect that models incorporating both of those constraints would be less susceptible to the systematic bias of a truncated mass profile. The lowest magnification estimate in our sample (from the Merten model) is among this sub-sample. However, we find that collectively these three strong+weak models (shown as diamonds in Figure 7) exhibit the same propensity to overestimate the magnification along this line of sight. Thus, a sudden change in the mass profile outside the strong lensing region is not a likely explanation for this small systematic bias.

With two versions of the CATS model, we also have a more direct test of the effect of introducing weak lensing constraints. The initial CATS model uses only strong-lensing constraints, and gives $\mu = 2.27^{+0.05}_{-0.04}$, slightly higher than the measured value. A second iteration of this model, labeled here as CATS-SL+WL, used the same strong-lensing features, but added in weak lensing constraints. The revised magnification of $\mu = 2.62 \pm 0.18$ is further from the measured value, which serves to reinforce the conclusion that adding weak lensing constraints cannot resolve this bias.

6.6. *Redshift Error*

If the redshift of the SN derived in Section 3 were incorrect, then one would derive a different value for the magnification, both from the SN measurement and the lens model predictions. Conceivably, this could resolve the tension between the measurement and the models. It is often the case in SN surveys that redshifts are assigned based on a host galaxy association, typically inferred from the projected separation between the SN and nearby galaxies. In this case the redshift evidence comes from the SN itself, and we find a consistent redshift from both the SN spectrum (Section 3.2) and the light curve Section 4, which are both within the 1σ range of the photometric redshift for the nearest detected galaxy: $z = 1.5 \pm 0.2$. This appears to be a solid and self-consistent picture, so the evidence strongly disfavors any redshift that is significantly different from $z = 1.3$.

We have adopted the spectroscopic redshift of $z = 1.31 \pm 0.01$ for the magnification comparison. Spectroscopic redshifts are generally more precise and accurate than those derived from photometric observations (Rodney & Tonry 2010; Kessler et al. 2010; Sako et al. 2011). However, in this case the spectrum is limited to the rest-frame near-UV wavelengths, where the available SN spectral template libraries are more limited than at optical wavelengths. If we use the photometric redshift of $z = 1.35 \pm 0.02$ instead, then the measured magnification is reduced.[11] From the SALT2 fitter we derive $\mu_{\rm SALT2} = 1.80 \pm 0.30$ and from MLCS2k2 we get $\mu_{\rm MLCS2k2} = 1.83 \pm 0.17$. The lens models are also shifted, and they uniformly move in the opposite direction, to magnification values that are *larger* than at $z = 1.31$, by $\sim 1\%$. Thus, shifting the SN to the photometric redshift of $z = 1.35$ only serves to (slightly) exacerbate the tension between the observations and models.

[11] By increasing the redshift, the SN is presumed to be at a greater distance, so to first order one would be expect it to appear slightly fainter (larger distance modulus). If the distance modulus inferred from the light curve fit remained constant, this would drive the inferred magnification to a higher value. However, the light curve fitting is more strongly affected by the covariance between redshift, color, and light curve width. In this case, these effects drive the distance modulus to a larger value at $z = 1.35$, resulting in a smaller value of the observed magnification μ.

6.7. *Foreground Dust*

All SN sight-lines must intersect some amount of foreground dust from the immediate circumstellar environment, the host galaxy, and the intergalactic medium (IGM). In the case of SN HFF14Tom one might posit some dust extinction from the intra-cluster medium (ICM) of Abell 2744, although measurements of rich clusters suggest that the ICM has only a negligible dust content (???). When fitting the HFF14Tom light curve we account for dust by including corrections that modify the inferred luminosity distance based on the SN color. If after applying these dust corrections we are still *underestimating* the effect of dust along this sight-line, then the SN would appear more dim, the inferred distance modulus would be higher, and the measured magnification would be reduced – consistent with the discrepancy we observe.

One might suppose that a bias could be introduced if we have adopted incorrect values for the color correction parameter β or extinction law R_V in the SALT2 and MLCS2k2 fits, respectively. The appropriate value to use for this color correction and how it affects inferences about the intrinsic scatter in Type Ia SN luminosities is a complex question that is beyond the scope of this work (see e.g. Marriner et al. 2011; Chotard et al. 2011; Kessler et al. 2013; Scolnic et al. 2014). However, we can already rule this out as a solution for the magnification discrepancy. Our error on the HFF14Tom distance modulus already includes an uncertainty in the extinction law and a related error to account for the intrinsic luminosity scatter. These are well vetted paraemeters, based on observations of ~ 500 SNe extending to $z \sim 1.5$ (Sullivan et al. 2011). Furthermore, changing the color correction applied to SN HFF14Tom would requre the same adjustment to be applied to the unlensed SNe at similar redshift that make up our comparison sample, unless one proposes without evidence that SN HFF14Tom is uniquely affected by a peculiar type of dust.

The traditional color corrections as formalized in SN light curve fitters are designed to account for a dust component that lies in the rest frame of the SN. The inferred luminosity of a SN can also be affected by the presence of foreground dust with a different redshift and possibly a different reddening law (?). However, the magnitude of such a bias is insufficient to account for the observed discrepancy, ? estimate the opacity of the universe as $\langle A_V \rangle \sim 0.03$ mag up to $z = 0.5$. While this can have a measurable impact on precise cosmological constraints, it is far less than the 0.285 mag difference between the observed magnification of HFF14Tom and the mean of the model predictions.

7. MISCLASSIFICATION

TODO : discuss 2006bt-like misclassification

In Section 5 we found that SN HFF14Tom is on the blue end of the normal range of Type Ia SN colors. With the SALT2 fitter we measured a color parameter $c = -0.115 \pm 0.025$, and with MLCS2k2 we found the host galaxy dust extinction to be $A_V = 0.014 \pm 0.037$ magnitudes. These colors are tightly constrained, as we are fitting to photometry that covers a rest-frame wavelength range from $\sim 3500-7000$Åand extends to ∼30 days past maximum brightness. This makes it difficult to invoke an error in the host galaxy dust correction as an explanation for the magnification discrepancy.

8. SUMMARY AND CONCLUSIONS

The appearance of a Type Ia SN behind a massive galaxy cluster provides a rare opportunity to use a standard candle for a direct measurement of the absolute magnification due to gravitational lensing. The discovery of SN HFF14Tom in the HFF imaging of Abell 2744 offers the first chance to apply this test on a cluster with multiple publicly-available lens models. We have found that the spectrum and light curve of SN HFF14Tom are well matched by templates of a normal Type Ia SN at $z = 1.31 \pm 0.01$. Using the two most prevalent SN Ia light curve fitters, SALT2 and MLCS2k2, we get a consistent measurement of the distance modulus (Table 2). Using a cosmology-independent comparison against a sample of unlensed SNe Ia at similar redshifts, we find that SN HFF14Tom is ~ 0.7 magnitudes brighter than the field sample would predict. Attributing this difference to the gravitational lensing magnification (and accounting for the intrinsic scatter in luminosity of the SN Ia population), we have derived a consistent measured magnification of $\mu_{\rm SALT2} = 1.89 \pm 0.29$. $\mu_{\rm MLCS2k2} = 2.00 \pm 0.19$, from the two light curve fitters.

Taking advantage of the availability of eleven well-constrained lens models for the Abell 2744 cluster, we have used SN HFF14Tom to ask how accurately these lens models can predict the magnification along this line of sight. We find that these models are consistent, and fairly accurate, collectively predicting $\mu = 2.60 \pm 0.34$. This is encouraging, and reinforces the quality and value of these public lens models for studying magnified background objects. However, the fact that all models predict a larger magnification value than we observe is an indication that there is a small systematic bias inherent to this cluster or sight-line.

We have speculated on the origin of this systematic bias, evaluating five possible causes:

1. The close proximity of a cluster member galaxy is leading to a biased magnification, because that galaxy's M/L is atypical.

2. The models are limited by a scarcity of strong lensing constraints

3. The cluster mass profile exhibits a sudden change outside of the core strong-lensing region, where we lack multiply-imaged background sources to constrain it.

4. **The redshift assigned to SN HFF14Tom is in error.**

5. **The color corrections for SN HFF14Tom underestimate the foreground dust.**

6. **SN HFF14Tom is not a normal Type Ia SN.**

The first three of these take on the discrepancy from the lens modeling side, but none are completely satisfactory. For each of these scenarios, we would expect that certain subsets of the available lens models would be less sensitive to the proposed systematic bias. However, the small discrepancy between the predicted and observed lensing magnification is persistent when we bifurcate the sample of lens models according to methodology (parametric vs. free-form), number of strong-lensing constraints (pre-vs post-HFF), and scope of lensing constraints (strong-lensing only vs. strong+weak). Thus, comparison of the available models does not provide any definitive explanation for this magnification tension.

The last two possible explanations presume an error in the interpretation of the available SN data. We reject the possibility that a redshift error is the primary cause of the discrepancy, as the redshift evidence is derived principally from the SN itself and not from the host galaxy. A value of $z \sim 1.3$ is well supported by both the spectroscopic and photometric SN data, and changing the redshift within the constraints of these complementary observations only serves to increase the tension between the observed and predicted magnifications.

Finally, we have considered whether the SN could be mis-classified. Once again the combination of spectroscopic and photometric evidence strongly supports our classification of SN HFF14Tom as a normal Type Ia SN. The most plausible mis-classification would be that the object is a peculiar Type Ia of the SN 2006bt-like sub-class. We find this possibility to be TODO: summarize the 06bt misclassification discussion

This single object behind a single cluster is not in and of itself a cause for alarm. Previous analyses of lensed SN Ia found no significant discrepancy beween the observed SN Ia magnifications and the predictions from lens models (P14; Nordin et al. 2014), albeit with a much smaller set of lens models being tested. The observed systematic bias for HFF14Tom is small, and many of the lens models being evaluated are preliminary models that have not been updated to include all of the HFF data. Future revisions of the lens models for Abell 2744 should either incorporate the observed magnification of HFF14Tom as a new model constraint, or can revisit this test to evaluate whether the bias persists.

A promising avenue for exploring the origins of systematic biases in cluster lens models is through the use of simulated data. One can start with very deep high-resolution multi-band imaging on an unlensed field that has a fairly complete spectroscopic redshift catalog, such as the Hubble Ultra Deep Field. Then a simulated galaxy cluster is placed in the field, and the background galaxies are distorted into arcs and multi-

ple images using a well-defined lensing prescription. The artificially lensed images can then be distributed to lens modeling teams who attempt to reconstruct the (known) mass profile of the simulated cluster. This exercise has recently been pursued with a set of synthetic clusters similar to those observed in the HFF program (Meneghetti et al. in prep). Preliminary analysis of this simulation comparison suggests that systematic biases such as we have seen for SN HFF14Tom may be common for sources that lie close to the critical curve in elongated and highly asymmetric clusters like Abell 2744. This SN analysis indicates that such simulation efforts will be an important step for moving toward precision science with cluster-lensed sources.

Increasing the sample of SNe behind well studied strong lensing clusters would allow this test to be repeated and refined. With 10 or 100 such objects, it would be possible to see whether the SN HFF14Tom μ discrepancy is simply an outlier, or an indication of a more pernicious systematic error. Any cluster that has been vetted by pencil-beam magnification tests using lensed SN Ia will be able to provide a more reliable measure of the magnifications for very high redshift objects. Similarly, a broad sample of SNe like HFF14Tom would help to define the preferred lens modeling methodology by highlighting any models that consistently perform well in SN Ia lensing tests. The ongoing FrontierSN program will discover and follow any more highly magnified SNe that appear behind the Frontier Field clusters. Unfortunately, the HFF survey is not designed with high-z transient discovery as a primary science goal, so the FrontierSN effort will likely add no more than 1-3 new lensed SN Ia. Further imaging of strong-lensing clusters with *HST* or the James Webb Space Telescope (JWST) could enable a larger sample to be collected, especially if the filters and cadence are optimized for detection of SN Ia at $z > 1$. Massive clusters such as Abell 2744 will continue to be attractive as cosmic telescopes, allowing the next generation of telescopes to reach the faintest objects in the very early universe. The puzzling bias revealed by SN HFF14Tom supports a concerted effort to improve these lenses with a larger sample of magnified SNe.

Acknowledgments:

This work is dedicated to our colleague and friend Tomas Dahlen (-2014), for whom this supernova has been named in memorium. He is greatly missed.

We thank the Hubble Frontier Fields team at STScI for their substantial efforts to make the HFF program successful. In particular, thanks are due to Matt Mountain for the allocation of discretionary orbits for the HFF program; to Jennifer Lotz, Norman Grogin and Patricia Royle for accommodations in strategy and implementation to make the FrontierSN program possible; and to Dan Coe for curating the excellent and accessible lens model comparison tools. We also must thank the CLASH team, led by Marc Postman, for observations, catalogs, and high level science products that were of significant value for this analysis.

Financial support for this work was provided to SAR by NASA through grants HST-HF-51312 and HST-GO-13386 from the Space Telescope Science Institute, which is operated by Associated Universities for Research in Astronomy, Inc., under NASA contract NAS 5-26555.

Support for this research at Rutgers University was provided in part by NSF CAREER award AST-0847157 to SWJ. The Dark Cosmology Centre is supported by the Danish National Research Foundation.

J.M.D acknowledges support of the consolider project CAD2010-00064 and AYA2012-39475-C02-01 funded by the Ministerio de Economia y Competitividad.

J.M. contributed to this research from the Jet Propulsion Laboratory, California Institute of Technology, under a contract with NASA and acknowledges support from NASA Grants HST-GO-13343.05-A and HST-GO-13386.13-A. The research leading to these results has received funding from the People Programme (Marie Curie Actions) of the European Union's Seventh Framework Programme (FP7/2007-2013) under REA grant agreement number 627288.

Facilities: HST (WFC3)

REFERENCES

Benítez, N. 2000, ApJ, 536, 571
Blondin, S., & Tonry, J. L. 2007, ApJ, 666, 1024
Bradač, M., Lombardi, M., & Schneider, P. 2004, A&A, 424, 13
Bradač, M., et al. 2005, A&A, 437, 39
—. 2009, ApJ, 706, 1201
Brammer, G. B., et al. 2012, ApJS, 200, 13
Chotard, N., et al. 2011, A&A, 529, L4
Coe, D., et al. 2013, ApJ, 762, 32
Conley, A., et al. 2011, ApJS, 192, 1
—. 2008, ApJ, 681, 482
Falco, E. E., Gorenstein, M. V., & Shapiro, I. I. 1985, ApJ, 289, L1
Fruchter, A. S., et al. 2010, in STSCI Calibration Workshop Proceedings, Baltimore, MD, 21-23 July 2010, ed. S. D. . C. Oliveira (Space Telescope Science Institute), 376
Goobar, A., et al. 2009, A&A, 507, 71
Graur, O., et al. 2014, ApJ, 783, 28
Guy, J., et al. 2010, A&A, 523, A7
Holtzman, J. A., et al. 2008, AJ, 136, 2306
Holz, D. E. 2001, ApJ, 556, L71
Ishigaki, M., et al. 2015, ApJ, 799, 12
Jauzac, M., et al. 2014a, MNRAS, 443, 1549
—. 2012, MNRAS, 426, 3369
—. 2014b, arXiv:1409.8663
Jha, S., Riess, A. G., & Kirshner, R. P. 2007, ApJ, 659, 122
Johnson, T. L., et al. 2014, ApJ, 797, 48
Jones, D. O., et al. 2013, ApJ, 768, 166
Jullo, E., & Kneib, J.-P. 2009, MNRAS, 395, 1319
Jullo, E., et al. 2007, New Journal of Physics, 9, 447
Kessler, R., et al. 2010, PASP, 122, 1415
—. 2009a, ApJS, 185, 32
—. 2009b, PASP, 121, 1028
—. 2013, ApJ, 764, 48
Lam, D., et al. 2014, ApJ, 797, 98
Landsman, W. B. 1993, in Astronomical Society of the Pacific Conference Series, Vol. 52, Astronomical Data Analysis Software and Systems II, ed. R. J. Hanisch, R. J. V. Brissenden, & J. Barnes, 246
Li, W., et al. 2011, MNRAS, 412, 1441
Liesenborgs, J., De Rijcke, S., & Dejonghe, H. 2006, MNRAS, 367, 1209
Liu, Y., & Modjaz, M. 2014, arXiv:1405.1437
Marriner, J., et al. 2011, ApJ, 740, 72
Merten, J., et al. 2009, A&A, 500, 681
—. 2011, MNRAS, 417, 333
Mohammed, I., et al. 2014, MNRAS, 439, 2651
Navarro, J. F., Frenk, C. S., & White, S. D. M. 1997, ApJ, 490, 493
Nordin, J., et al. 2014, MNRAS, 440, 2742
Oguri, M. 2010, PASJ, 62, 1017

Patel, B., et al. 2014, ApJ, 786, 9
Quimby, R. M., et al. 2014, Science, 344, 396
Rest, A., et al. 2014, ApJ, 795, 44
Richard, J., et al. 2014, MNRAS, 444, 268
Riehm, T., et al. 2011, A&A, 536, A94
Riess, A. G., & Livio, M. 2006, ApJ, 648, 884
Rodney, S. A., et al. 2014, AJ, 148, 13
Rodney, S. A., & Tonry, J. L. 2010, ApJ, 723, 47
Sako, M., et al. 2011, ApJ, 738, 162
Scolnic, D., et al. 2014, ApJ, 795, 45
Sendra, I., et al. 2014, MNRAS, 2642
Smartt, S. J., et al. 2009, MNRAS, 395, 1409
Sonnenfeld, A., Bertin, G., & Lombardi, M. 2011, A&A, 532, A37
Stetson, P. B. 1987, PASP, 99, 191
Sullivan, M., et al. 2011, ApJ, 737, 102
Suzuki, N., et al. 2012, ApJ, 746, 85
Tonry, J., & Davis, M. 1979, AJ, 84, 1511
Treu, T. e. a. ????, in prep
Zheng, W., et al. 2012, Nature, 489, 406
Zitrin, A., et al. 2009, MNRAS, 396, 1985
—. 2013, ApJ, 762, L30